Weierstraß–Institut
für Angewandte Analysis und Stochastik

im Forschungsverbund Berlin e.V.

Preprint ISSN 0946 – 8633

Modeling and Simulation of Strained Quantum Wells in Semiconductor Lasers

Uwe Bandelow[1], Hans–Christoph Kaiser[1], Thomas Koprucki[1], and

Joachim Rehberg[1]

submitted: 19 May 2000

[1] Weierstraß-Institut
für Angewandte Analysis und Stochastik
Mohrenstraße 39
D–10117 Berlin
Germany
E-Mail: bandelow@wias-berlin.de
E-Mail: kaiser@wias-berlin.de
E-Mail: koprucki@wias-berlin.de
E-Mail: rehberg@wias-berlin.de

Preprint No. 582
Berlin 2000

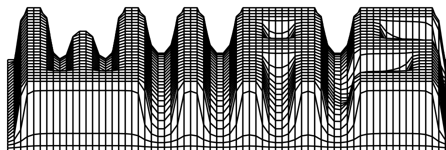

2000 *Mathematics Subject Classification.* 78A60, 68U20, 65Z05.

Key words and phrases. Quantum well laser, band structure, kp–method, Schrödinger–Poisson systems, exchange–correlation effects, optical gain, semiconductor laser simulation.

Edited by
Weierstraß–Institut für Angewandte Analysis und Stochastik (WIAS)
Mohrenstraße 39
D — 10117 Berlin
Germany

Fax: + 49 30 2044975
E-Mail (X.400): c=de;a=d400-gw;p=WIAS-BERLIN;s=preprint
E-Mail (Internet): preprint@wias-berlin.de
World Wide Web: http://www.wias-berlin.de/

Abstract

A model allowing for efficiently obtaining band structure information on semiconductor Quantum Well structures will be demonstrated which is based on matrix-valued **kp**-Schrödinger operators. Effects such as confinement, band mixing, spin-orbit interaction and strain can be treated consistently. The impact of prominent Coulomb effects can be calculated by including the Hartree interaction via the Poisson equation and the bandgap renormalization via exchange-correlation potentials, resulting in generalized (matrix-valued) Schrödinger-Poisson systems. Band structure information enters via densities and the optical response function into comprehensive simulations of Multi Quantum Well lasers. These device simulations yield valuable information on device characteristics, including effects of carrier transport, waveguiding and heating and can be used for optimization.

1999 Physics and Astronomy Classification Scheme (PACS):

42.55.Px, 73.20.Dx, 85.60.Bt, 78.66.Fd.

Contents

1 Introduction **2**

2 Quantum States **3**

2.1 Multi Quantum Wells 4

2.2 Single Quantum Wells 6

2.3 Transition Matrix Elements 6

2.4 Carrier Densities and Optical Response Function 6

2.5 Selfconsistent Quantum States 7

3 Device Simulation **10**

3.1 Optics 11

3.2 Heating 12

4 Summary **13**

1 Introduction

Semiconductor lasers are the most promising optoelectronic devices for generation of intense light in very small spectral domains. With emission wavelengths ranging now from near UV to far IR, these laser diodes are used in a wide range of applications. Their operating state is usually characterized by conduction bands occupied with electrons and valence bands occupied with holes which are separated by an energy gap. Emission of light, the wavelength of which is roughly given by this bandgap, results from recombination of electron-hole pairs. Applications depending on proper adjustment of the emission wavelength require bandgap engineering.

Laser action requires optical gain, the description of which is the heart of semiconductor laser modeling. The gain corresponds to the imaginary part of the optical response function, which itself depends on almost all properties of the semiconductor material and the operating state of the device as well as on properties of the optical field, e.g. its wavelength and polarization. To increase the gain in a laser, carriers and photons should be confined together in a small (optical active) region (see Fig. 1), requiring semiconductor heterostructures, in general nanostructures. During the last decade sophisticated Quantum Well structures have been developed to achieve good confinement and high optical gain. This has been done by band structure engineering, using in particular geometry, band offset and strain. Widely applied, Strained Multi Quantum Wells (SMQW) are subject to intense research – as in this project.

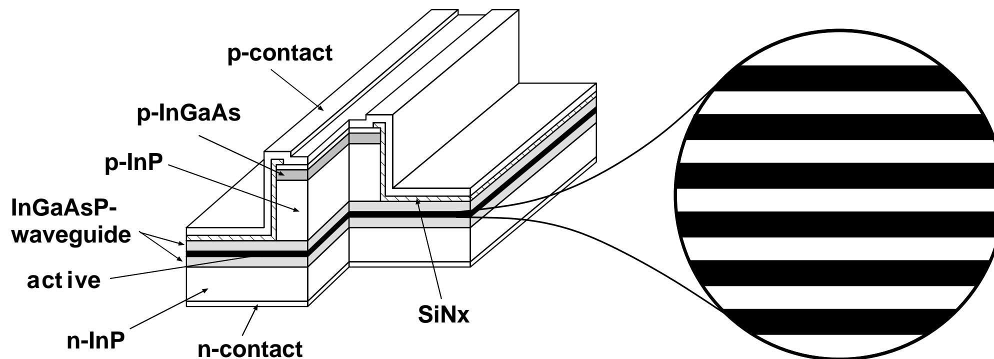

Figure 1: Scheme of a Ridge-Waveguide (RW) Strained Multi Quantum Well (SMQW) laser diode, by Heinrich–Hertz–Institut für Nachrichtentechnik, Berlin. By forward biasing the diode, holes are injected from the p-contact, electrons from the n-contact, and get confined in the optical active SMQW region, which is enlarged on the right. Supported by the waveguide layers and the ridge optical modes are guided along the active region to achieve a significant optical gain.

For state of the art optoelectronic devices mainly two material classes are important which differ in their crystal symmetry: cubic and wurtzite. Cubic materials can be found in long wavelength lasers based on e.g. Indium Phosphide (InP) and/or

Gallium Arsenide (GaAs). The more recent blue/UV diode lasers are based on Gallium Nitride (GaN), usually grown in wurtzite configuration. Gain spectra for a cubic (left) and a wurtzite material system (right) are drawn in Fig. 2, calculated with KPLIB[1]. The optical response is extremely sensitive to the electronic band

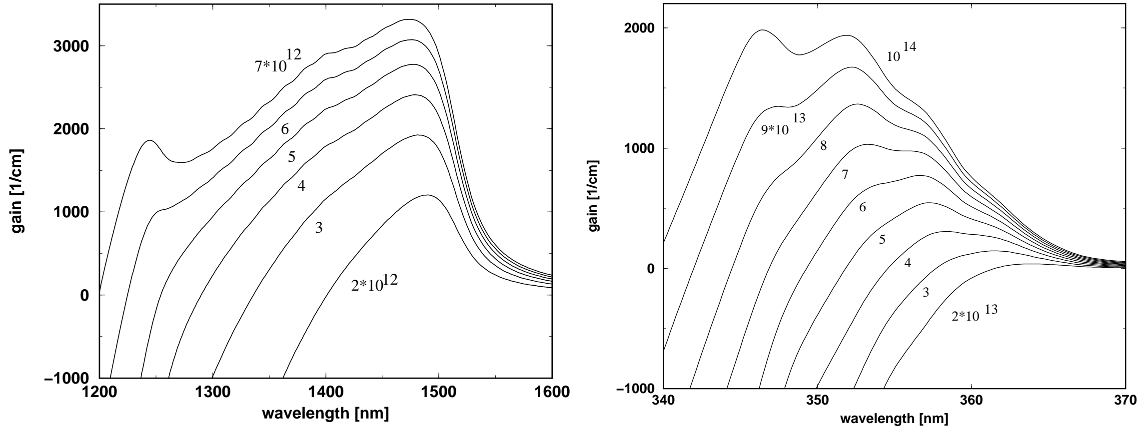

Figure 2: Examples of material gain dispersion in Strained Quantum Wells at room temperature for different sheet concentrations. Left: InGaAsP, Right: AlGaN/GaN.

structure and to the transition matrix elements. The calculation of these quantities for the optical active SMQW region (see Fig. 1) will be subject of section 2. We have used these data for predicting the characteristics of devices as drawn in Fig. 1. Corresponding models and simulation results will be presented in section 3.

Throughout this paper our example device is the SMQW-laser depicted in Fig. 1. It is a 470μm long single section Fabry–Perot laser with cleaved facets, designed for emitting at 1.55 μm. The optical active region (enlarged on the right of Fig. 1) consists of six 7nm thick compressively strained Quantum Wells, sandwiched by 10nm thick tensile strained barriers.

2 Quantum States

Strained Multi Quantum Wells give rise to strong *band mixing effects*. These affect not only the Density of States, but also the transition matrix elements between these states and hence the optical response function.

We treat band mixing effects based on **kp**-calculations with the quantum states $\Psi_{l,\mathbf{k}_\|}(\mathbf{r})$ described within the Envelope Function Approach:

$$\Psi_{l,\mathbf{k}_\|}(\mathbf{r}) = \exp(i\mathbf{k}_\|\mathbf{r}_\|)\sum_\nu F_{\nu l}(z;\mathbf{k}_\|)u_{\nu,\mathbf{k}=0}(\mathbf{r}). \tag{1}$$

The index $\|$ indicates in-plane vectors and z denotes the quantization direction. The $u_{\nu,\mathbf{k}=0}(\mathbf{r})$ are zone-center Bloch functions, varying on the atomic scale, $F_{\nu l}(z;\mathbf{k}_\|)$ are

envelope functions, varying on the nanoscale. Based on the conventional **kp** method [2, ch.4] applied here this approach yields a matrix Hamiltonian

$$H_{\mu\nu}\left(\mathbf{k}_{\|}, k_z = -i\frac{\partial}{\partial z}, V(z), \epsilon\right).$$

In this simple form this **kp**-*Schrödinger operator* covers the crystal symmetry and the spin-orbit interaction, expressed by measurable Luttinger parameters, the confinement $V(z)$ imposed by the band offsets of the adjacent materials, and the impact of strain ϵ induced by their different solitary lattice constants.

The envelope functions $F_{\nu l}$ of the quantum states and the corresponding subband dispersions $E_l(\mathbf{k}_{\|})$ are solutions of the respective eigenvalue problem

$$\sum_{\nu} H_{\mu\nu}\left(\mathbf{k}_{\|}, k_z = -i\frac{\partial}{\partial z}; \ldots\right) F_{\nu l}(z; \mathbf{k}_{\|}) = E_l(\mathbf{k}_{\|}) F_{\mu l}(z; \mathbf{k}_{\|}). \tag{2}$$

In KPLIB [1], we have implemented several stages in the hierarchy of **kp**-models. The simplest stage applies to Light Hole (LH) – Heavy Hole (HH) band mixing based on a 4x4 matrix Hamiltonian. Additional coupling to Spin-Split Off (SO) bands enlarges the problem to a 6x6 matrix Hamiltonian. Both are purely valence-band Hamiltonians valid for describing the hole dispersion to some extent. Valence-band (VB) Hamiltonians are mathematically advantageous, because they are always semibounded [3].

For consistently modeling mixing of conduction and valence bands we use 8x8 Hamiltonians. This causes nonparabolic dispersion for the conduction subbands as well and allows for consistently predicting optoelectronic properties. 8x8 Hamiltonians are not semibounded and their mathematical and numerical treatment is much more difficult, because standard comparison arguments for eigenvalues do not apply. Indeed, spurious solutions and their elimination are discussed in the literature [4]. We have performed a spectral analysis [3], showing, that spurious solutions don't appear if the interband coupling remains weak enough. This is the case in wide gap materials as GaN, whereas GaAs and InP based materials are situated close above this limit.

2.1 Multi Quantum Wells

We have investigated the Multi Quantum Wells based on (8x8) **kp**-calculations. With decreasing barrier width the states localized in the individual Quantum Wells start to couple with each other which gives rise to miniband formation. We have studied this behaviour, which is illustrated in Fig. 3. In our example, no dispersion is observed for the lowest conduction and highest valence minibands, which contribute most to the optical response. This is a typical feature, indicating a good laser design for achieving small linewidths in the laser emission. In such cases we may confine to the single quantum well case, which considerably reduces the numerical effort. As is visible in Fig. 3, the other minibands exhibit dispersion, corresponding to less localized states which interfere in Multi Quantum Wells.

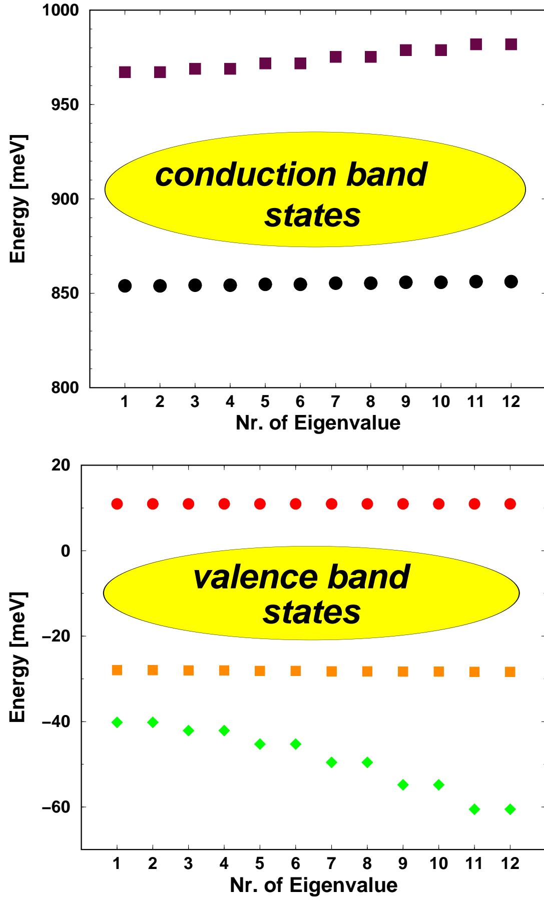

Figure 3: Miniband formation in a SMQW structure consisting of 6 Quantum Wells. Due to symmetry all eigenvalues are twice degenerate, yielding groups of 12 eigenvalues.

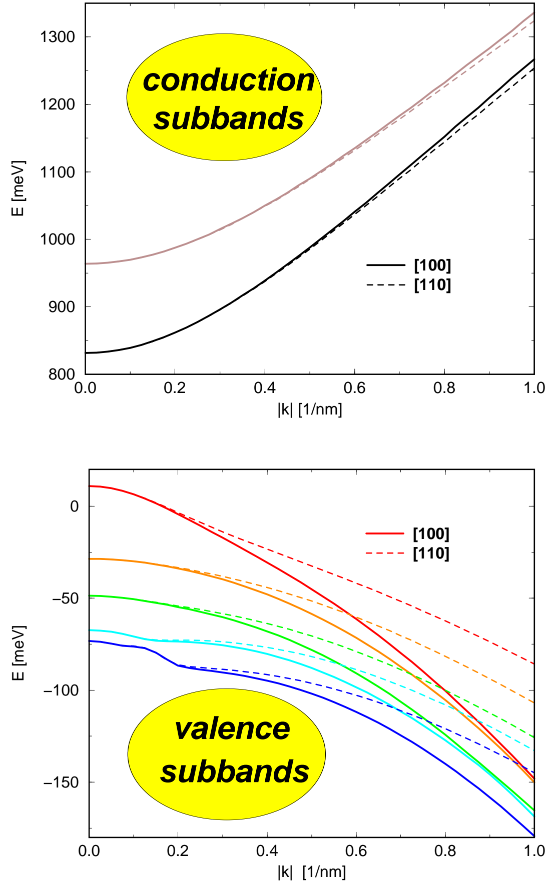

Figure 4: Subband dispersion and warping in a 7nm InGaAsP compressively strained Quantum Well, calculated with KPLIB for different crystallographic directions in the $\mathbf{k}_{||}$ plane.

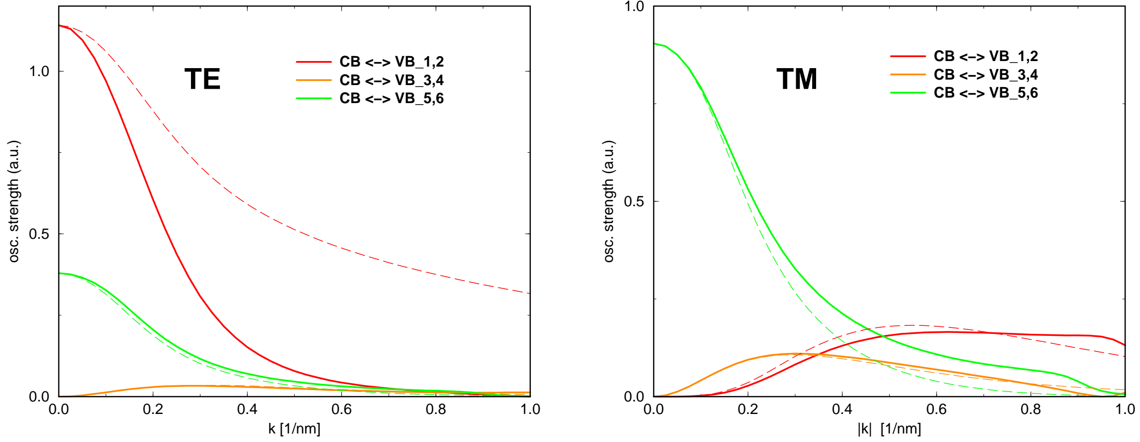

Figure 5: Interband oscillator strength dispersion for transitions between the lowest conduction subband and the upper valence subbands for different crystallographic directions, corresponding to Fig. 4, for TE– and TM–polarization.

2.2 Single Quantum Wells

The conduction and valence subband dispersion $E_l(\mathbf{k}_\|)$ for our example Quantum Well is drawn in Fig. 4. Due to the compressive strain in the Quantum Well the LH-HH degeneracy at $\mathbf{k} = 0$ is lifted, and the upper two valence subbands correspond to HH-like states. The dispersion is shown for two different crystallographic directions ([100] and [110]) in the $\mathbf{k}_\|$-plane, which exhibits the warping (angular dependence) effect. Fig. 4 displays weak warping for conduction subbands, but strong warping for the valence subbands.

2.3 Transition Matrix Elements

Taking the $\mathbf{k}$-gradient of $H_{\mu\nu}(\mathbf{k};\ldots)$ and the solutions $F_{\nu i} = F_{\nu i}(z;\mathbf{k}_\|)$ of (2) we get the *momentum matrix elements* $\mathbf{p}_{ij} = \mathbf{p}_{ij}(\mathbf{k}_\|)$:

$$\mathbf{p}_{ij} = \frac{m_0}{\hbar}\sum_{\mu,\nu}\left\langle F_{\mu i}\middle|\nabla_{\mathbf{k}}H_{\mu\nu}\left(\mathbf{k}_\|,k_z;\ldots\right)\Big|_{ik_z=\frac{\partial}{\partial z}}\middle|F_{\nu j}\right\rangle, \tag{3}$$

(m_0 = free electron mass) which quantify the transition rate between the states involved under presence of optical excitation. This transition rate enters, e.g., the optical gain, expressed by (7). The corresponding oscillator strengths for our quantum well are depicted in Fig. 5, both for the TE-polarized ($\mathbf{p}_{ij} \perp \mathbf{e}_z$) and the TM-polarized case ($\mathbf{p}_{ij} \parallel \mathbf{e}_z$). Obviously, the TE-polarization is favoured by our particular structure, which is due to the support for the CB-HH like transitions by the compressive strain in the wells (see Fig. 4). Especially for the main transitions we have to state a strong influence of warping and it should be noted that calculations restricted to only [100] or [110] directions are expected to give wrong results for the response functions.

2.4 Carrier Densities and Optical Response Function

If the Fermi levels ϕ_n and ϕ_p of the quantum confined electrons n and holes p are given, or, alternatively, their sheet concentrations, then the quantum confined carrier densities are obtained by

$$n(z) = \sum_{l\in c}\int\frac{d^2\mathbf{k}_\|}{(2\pi)^2}f\Big(E_l(\mathbf{k}_\|)-\phi_n\Big)\sum_\nu|F_{\nu l}(z;\mathbf{k}_\|)|^2, \tag{4}$$

$$p(z) = \sum_{l\in v}\int\frac{d^2\mathbf{k}_\|}{(2\pi)^2}\Big(1-f\Big(E_l(\mathbf{k}_\|)-\phi_p\Big)\Big)\sum_\nu|F_{\nu l}(z;\mathbf{k}_\|)|^2 \tag{5}$$

with the Fermi distribution

$$f(E) = \left(1+\exp\left(\frac{E}{k_BT}\right)\right)^{-1}, \tag{6}$$

where k_B denotes the Boltzmann constant and T the temperature. An example for the corresponding density distributions in our quantum well structure is shown in Fig. 7.

In addition, we can calculate the optical response function ε_{opt}. In our model the real part of ε_{opt}, which corresponds to the (squared) refractive index, consists of different contributions, stemming from a background as well as from interband and intraband transitions which are calculated according to Wenzel et. al. [5]. The resulting dispersion of the real part of ε_{opt} is shown for different sheet concentrations in the left part of Fig. 6. Besides a (frequency dependent) prefactor the interband contribution to the imaginary part of ε_{opt} corresponds to the material gain, which we have calculated according to [6]:

$$\begin{aligned} g(\omega) &= \frac{\pi\hbar q^2}{\varepsilon_0 m_0^2 n_r c} \frac{1}{L_z} \sum_{\substack{i\in c \\ j\in v}} \int \frac{d^2\mathbf{k}_\parallel}{(2\pi)^2} \frac{|\mathbf{p}_{ij}\mathbf{e}|^2}{E_i - E_j} f(E_i - \phi_n)\left(1 - f(E_j - \phi_p)\right) \times \\ &\quad \times \left[1 - \exp\left(\frac{\hbar\omega - (\phi_n - \phi_p)}{k_B T}\right)\right] \frac{1}{\pi} \frac{\Gamma}{\left[(E_i - E_j) - \hbar\omega\right]^2 + \Gamma^2}, \end{aligned} \tag{7}$$

where the last factor includes broadening processes, modeled with a characteristic intraband relaxation time τ of 60fs ($\Gamma = \hbar/\tau$). $\mathbf{e}$ is the polarization direction of the optical field, q denotes the elementary charge, c the speed of light, n_r the refractive index and L_z is a normalization length. Examples for the dispersion of the imaginary part of ε_{opt} are drawn in Fig. 6, which exhibit significant maxima, a prerequisite for laser action (see also the gain maxima in Fig. 2).

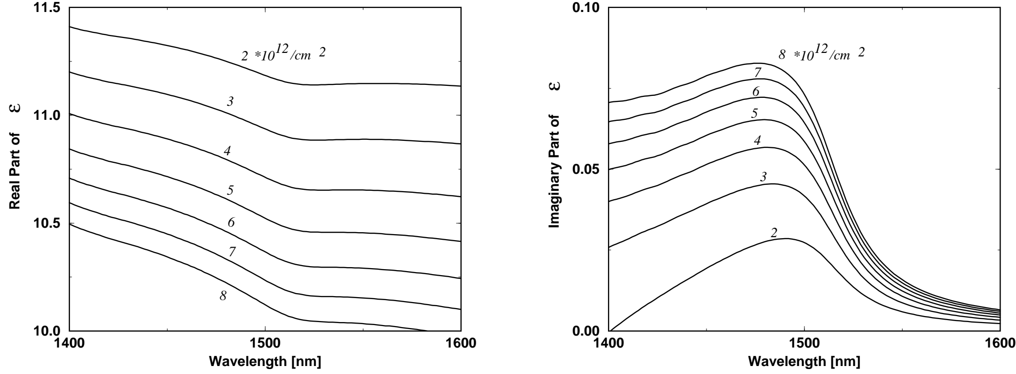

Figure 6: Dispersion of the real (left) and of the imaginary part (right: interband contribution only) of the optical response (TE-case) in a 7nm compressively strained InGaAsP Quantum Well for different sheet concentrations.

2.5 Selfconsistent Quantum States

The carriers are charged particles and therefore exert Coulomb interaction on each other which is additionally modified by their fermionic character. The Coulomb

interaction would guide us to much more complicated and nonlinear problems and results in important physical effects [7, ch.4] - the most prominent of which being the reduction of the bandgap to which we confine our analysis here. We include into our **kp**-model a Hartree potential and, motivated by the Density Functional Formalism [8], an exchange-correlation potential.

As can be seen from the thin lines in Fig. 7 the quantum confined carriers exhibit different localization behaviour in the Quantum Well, which is due to the different band offsets, Luttinger parameters and the presence of strain. In effect, an electrostatic potential builds up (see the full line in Fig. 8), which attracts the holes and repulses the electrons from the well in our particular case. Therefore we expect more equidistributed carriers than suggested by pure **kp**-calculations. This behaviour is covered by including the Hartree interaction into the **kp**-Schrödinger operator. The Hartree potential φ_H is a solution of the Poisson equation:

$$\frac{d}{dz}\left(\varepsilon\frac{d}{dz}\varphi_H\right) = q(n-p) \tag{8}$$

where the carrier densities according to (4),(5) enter the r.h.s., ε is the static dielectric permittivity. The arising system (2),(8) accomplished with (4),(5) can be viewed as a generalized (matrix-valued) Schrödinger-Poisson system. The bandgap shift now enters our model via density dependent exchange-correlation potentials $V_{xc}(n,p)$. Typical potentials are plotted in Fig. 8.

The mathematical analysis [9], [10] of the case without band mixing displays an unique solution for certain V_{xc}–potentials. Fortunately, in our example we also observed rapid convergence. In our particular case the wells and barriers are undoped. Therefore, we are close to the local charge neutrality $n = p$. For this case we have adopted a formula which is based on a result by Zimmermann [11] for parabolic bands:

$$V_{xc}^e = V_{xc}^h \propto \sqrt{\frac{n_s}{\sqrt{n_s + T/T_0}}}, \qquad n_s \propto \frac{n+p}{2}, \tag{9}$$

which is also valid for finite temperatures. Fig. 7 shows the impact of the Hartree-contribution together with the exchange-correlation effects on the density distributions.

Exchange-correlation effects enhance the tendency for localization of the carriers in the Quantum Well, uniformly for electrons and holes. At the chosen sheet concentration the exchange-correlation potential V_{xc} is approximately of the same amount as the Hartree potential (see Fig. 8). We have no net effect on the electrons because φ_H and V_{xc} nearly cancel each other, which is reflected in the similarity of the pure-**kp** (thin) and the selfconsistent (thick) electron density distribution curve in Fig. 7. For the holes the two potentials sum up to approximately twice the Hartree potential effect. This yields a strong enhanced localization for the holes, as reflected by the thick dashed curve in Fig. 7. The resulting net gap shrinkage of about 30meV is finally reflected in the shift of the gain spectrum in Fig. 9. The redshift, approximately 50nm, of the TE- as well as the TM-gain spectra corresponds very good to

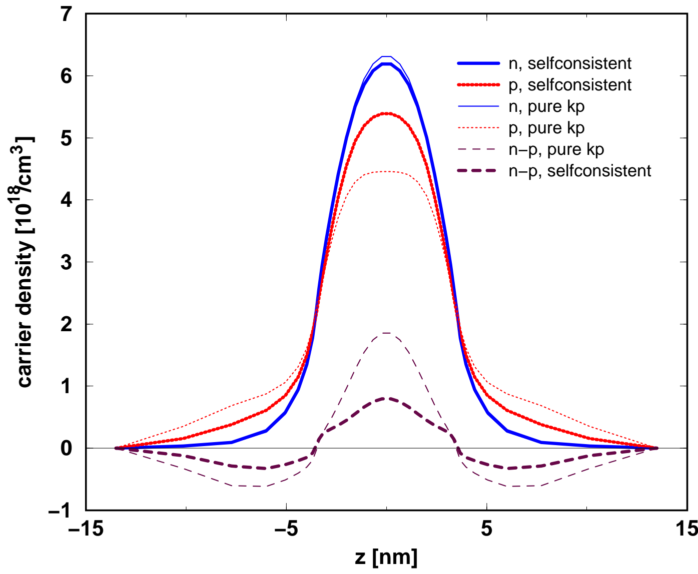

Figure 7: Density distribution in a 7nm Quantum Well, sandwiched between 10nm barriers for a sheet concentration of $4 \cdot 10^{12}/cm^2$. Thin: pure 8x8 **kp**. Thick: selfconsistent 8x8 **kp** with Hartree and exchange-correlation potential.

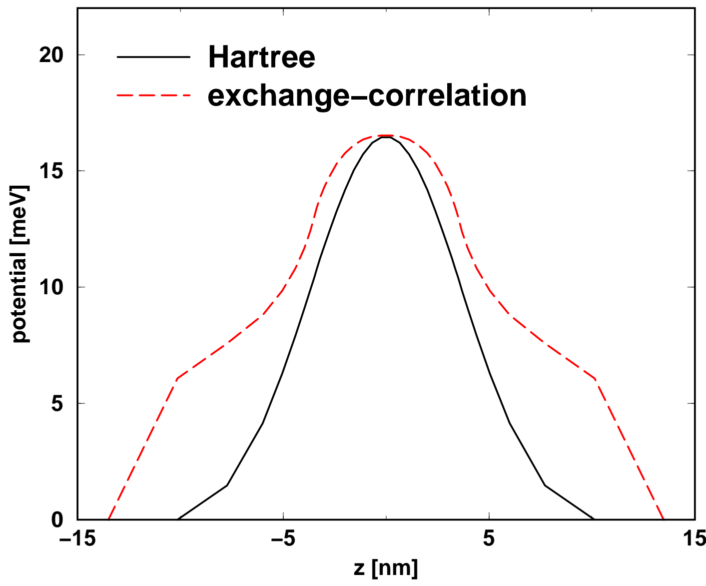

Figure 8: Spatial distribution of Hartree- and exchange-correlation potentials in a 7nm InGaAsP strained Quantum Well, selfconsistently calculated for a sheet concentration of $4 \cdot 10^{12}/cm^2$.

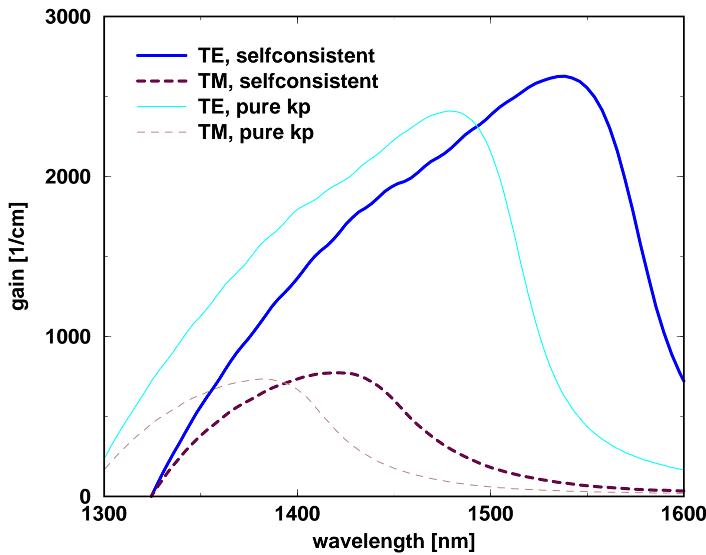

Figure 9: Spectrum of the material gain for TE- and TM polarization, corresponding to the case in Fig. 8. Thick: selfconsistent 8x8 **kp**, thin: pure 8x8 **kp**-calculations.

that value. The relative enhancement of the gain maxima visible in Fig. 9 reflects the more equidistributed electron- and hole wave functions, which results in a better overlap between them and hence increases the oscillator strength.

3 Device Simulation

A schematic overview on our simulations based on the packages KPLIB [1] and WIAS-TeSCA [12] is depicted in Fig. 10. The carrier transport is governed by

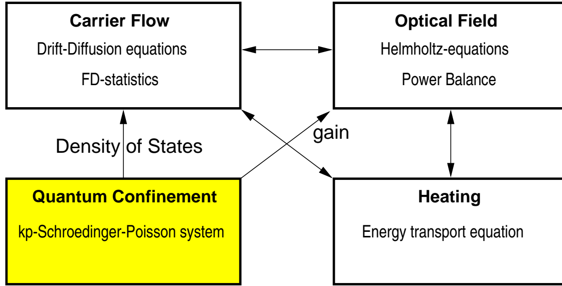

Figure 10: Schema of how the different models intertwine in our simulations. The treatment of carrier flow, optical field and heating is fully self-consistent, whereas the results of the **kp**-calculations (shaded module) enter parametrically via the Density of States and the optical gain.

Drift-Diffusion equations for electrons and holes:

$$q\frac{\partial}{\partial t}n - \nabla \mathbf{J}_n(n,\varphi) \quad = \quad qR \tag{10}$$

$$q\frac{\partial}{\partial t}p + \nabla \mathbf{J}_p(p,\varphi) \quad = \quad qR, \tag{11}$$

which are coupled to the Poisson equation for the electrostatic potential φ

$$-\nabla(\varepsilon\nabla\varphi) = q(N_D - N_A + p - n). \tag{12}$$

In the above equations $N_D - N_A$ is the net doping profile and R in (10),(11) is short for all recombination terms, which depend on the carrier densities, the electrostatic potential, the optical field and much other quantities. The relation between the carrier densities and the potentials is described by state equations in terms of Fermi-Dirac statistics

$$n = N_c \mathcal{F}_{1/2}\left(\frac{E_c + qF_n - q\varphi}{k_B T}\right), \quad p = N_v \mathcal{F}_{1/2}\left(\frac{qF_p - E_v - q\varphi}{k_B T}\right), \tag{13}$$

where E_c denotes the conduction and E_v the valence band edge. F_n and F_p are the quasi Fermi potentials of electrons and holes, the gradients of which drive the current densities $\mathbf{J}_n, \mathbf{J}_p$, respectively. $\mathcal{F}_{1/2}$ is the Fermi-integral of order 1/2.

According to (13) the carriers are treated bulk-like with band-edge Density of States N_c and N_v. For the quantum confined carriers the **kp**-calculations yield at least a modified Density of States N_c and N_v. In an advanced stage of the model the quantum confined carriers will be established as a separate species coupled to the free carriers by capture-escape mechanisms.

3.1 Optics

The above carrier equations are coupled to equations for the optical field. Due to properties of the laser resonator the latter are scalar Helmholtz equations (written here for TE modes)

$$\left[\Delta + \frac{\omega^2}{c^2}\varepsilon_{opt}(\omega, n, p)\right]\Phi_j = \beta_j^2 \Phi_j, \tag{14}$$

which describe the spatial distribution of the optical modes Φ_j within the simulation plane (see Fig. 11). These modes are characterized by their respective (complex) eigenvalues β_j. The imaginary part of $\varepsilon_{opt}(\omega, n, p)$ in (14) contains the material gain contribution, which is fitted to our (8x8) **kp**-calculations (see (7) and Fig. 6), as well as contributions from the Inter Valence Band Absorption (IVBA), described by phenomenological models in WIAS-TeSCA. As argued earlier and indicated by Fig. 9, we have strong support for the TE-polarization, but nearly no support for the TM-polarization in our structure. For this reason, calculations here are confined to TE modes, drawn in Fig. 11.

In 2D-simulations with WIAS-TeSCA, longitudinal properties are considered by assuming a longitudinally homogeneous power distribution, which is approximately met in Fabry-Perot lasers or in edge-emitting lasers with properly designed Bragg gratings [13]. In our calculations the two modes shown in Fig. 11 have been involved, the number of photons S_j of which are balanced by corresponding photon rate equations

$$\dot{S}_j = v_{g_j}(2\,\Im m\beta_j - \alpha_j)S_j + \dot{S}_j^{spont}, \tag{15}$$

where $\dot{S}_j^{spont}$ is short for the spontaneous emission into the mode, v_{g_j} denotes the modal group velocity, α_j is the sum of longitudinal scattering- and output losses at the facets and $\Im m\beta_j$ is the imaginary part of the corresponding eigenvalue subject to (14).

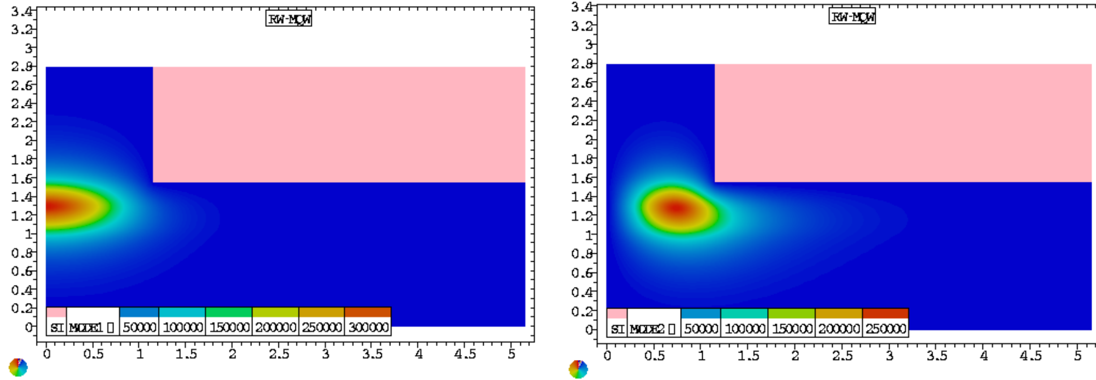

Figure 11: Intensity distribution of transverse TE-modes in a cross section of a RW-Laser as shown in Fig. 1, calculated with WIAS-TeSCA. Due to symmetry only the right half plane has been considered, which only partially is shown. Left: fundamental TE mode, right: 1st excited TE mode.

3.2 Heating

For a realistic estimation of the device performance heating effects are considered within the model. To that end WIAS-TeSCA comprises an energy transport equation [14], [15].

In Fig. 12 a stationary spatial temperature distribution for our example device is shown. The temperature of the heat sink was adjusted to room temperature (300K). The main heat source is located within the active region, corresponding to the profile of the main mode. Accordingly, we address the main heating processes to the IVBA.

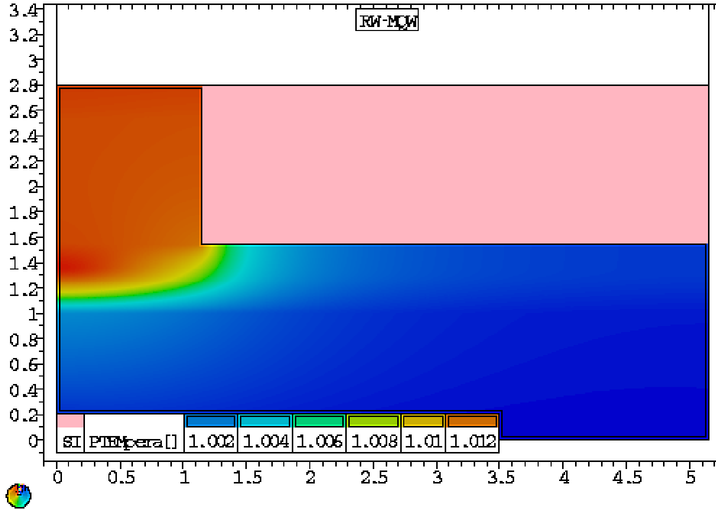

Figure 12: Temperature distribution, calculated with WIAS-TeSCA. I=27 mA, 3mW internal power. The maximum local heating is +3K in the active region, corresponding to the localization of the main mode (see Fig. 11) and can be mainly addressed to the IVBA.

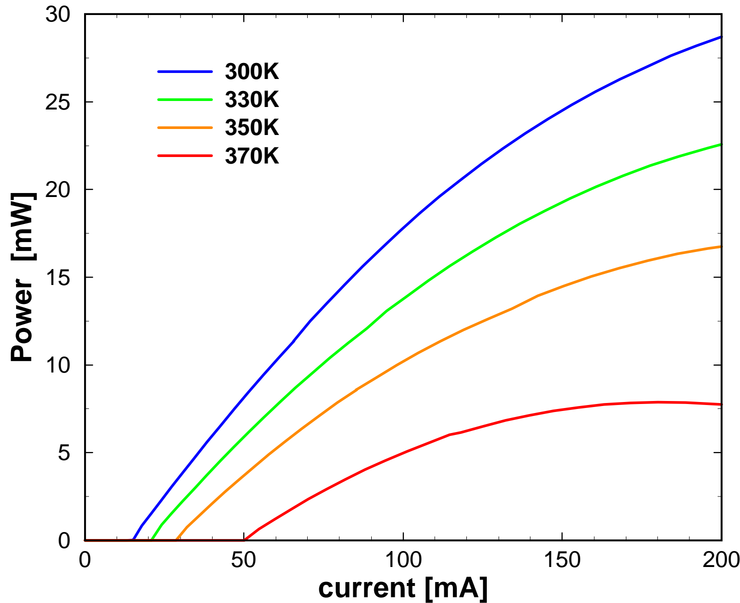

Figure 13: PI-characteristics of the SMQW-RW Laser, for heat sink temperatures from 300K to 370K. A significant thermal shift of the laser threshold is observed, as well as a thermal roll over at high temperatures, which corresponds to the experiments.

For estimating the thermal stability of the device operation we have studied the influence of different temperatures of the heat sink on the power-current (PI) charac-

teristics. Results of our simulations are shown in Fig. 13. Two important effects are observed, which are in agreement with the measurements. First, we can reproduce the significant shift of the laser threshold with temperature caused by decreasing material gain accompanied by an increase of IVBA. Due to these processes higher carrier densities are required for lasing, which enhances the recombination and therefore requires a larger threshold current (Fig. 13). Second, we can computationally reproduce a thermal roll-over at higher temperatures, which can be explained mainly by the significant increase of the Auger recombination which strongly decreases the quantum efficiency.

4 Summary

Many modern optoelectronic applications essentially rely on Quantum Well structures which need to be properly designed. Based on the Envelope Function Approach and **kp**-theory, a model has been developed which allows to simulate such structures consistently. Important information provided by the model are the non-parabolic band structure, the quantum confined states, their respective transition matrix elements, carrier densities and the optical response function, which is crucial for semiconductor laser modeling. Furthermore, this model has been extended for the Hartree interaction as well as for the density dependent bandgap shift to become as realistic as possible. Based on such results, more comprehensive device simulations have been performed. These simulations additionally included effects of carrier transport, doping, optical waveguiding and heating. The simulation results are in good agreement with the experiments, indicating their applicability for designing modern optoelectronic devices.

Acknowledgments

We acknowledge the cooperation with the Heinrich–Hertz–Institut für Nachrichtentechnik Berlin GmbH, in particular Martin Möhrle. We thank H. Wenzel (FBH Berlin) and H.-J. Wünsche (HU Berlin) for many fruitful discussions on laser modeling. Uwe Bandelow gratefully acknowledges the *German Federal Ministry for Education, Sciences, Research and Technology* for support of this work under grant no. 03-KA7FV1-4. The work of Thomas Koprucki has been supported by the *Deutsche Forschungsgemeinschaft* under grant no. HA 1807/5-1.

References

[1] T. Koprucki and U. Bandelow. KPLIB: An open tool box for the numerical treatment of $k \cdot p$ Schrödinger operators. WIAS Report, in preparation.

[2] S. L. Chuang. *Physics of optoelectronic devices*. Wiley&Sons, New York, 1995.

[3] U. Bandelow, H.-Chr. Kaiser, T. Koprucki, and J. Rehberg. Spectral properties of $k \cdot p$ Schrödinger operators in one space dimension. submitted to Numerical Functional Analysis and Optimization.

[4] B. A. Foreman. Elimination of spurious solutions from eight–band $k \cdot p$ theory. *Physical Review B*, 56:R12748–R12751, 1997.

[5] H. Wenzel, G. Erbert, and P. M. Enders. Improved theory of the refractive–index change in quantum–well lasers. *IEEE Journal of Selected Topics in Quantum Electronics*, 5(3):637–642, 1999.

[6] P.M. Enders. Enhancement and spectral shift of optical gain in semiconductors from non–markovian intraband relaxation. *IEEE Journal of Quantum Electronics*, 33(4):580–588, 1997.

[7] Weng W. Chow, Stephan W. Koch, and Murray Sargent III. *Semiconductor–Laser Physics*. Springer–Verlag, Berlin, 1994.

[8] R. M. Dreizler and E. K. U. Gross. *Density Functional Theory*. Springer–Verlag, Berlin, 1990.

[9] H.-Chr. Kaiser and J. Rehberg. About a one–dimensional stationary Schrödinger–Poisson system with Kohn–Sham potential. *Zeitschrift für Angewandte Mathematik und Physik (ZAMP)*, 50:423–458, 1999.

[10] H.-Chr. Kaiser and J. Rehberg. About a stationary Schrödinger–Poisson system with Kohn–Sham potential in a bounded two– or three–dimensional domain. *Nonlinear Analysis*, 41:33–72, 2000.

[11] R. Zimmermann. *Many–Particle Theory of Highly Exited Semiconductors*, volume 18 of *Teubner–Texte zur Physik*. BSB Teubner, Leipzig, 1988.

[12] H. Gajewski et al. TeSCA *Two– and three–dimensional SemiConductor Analysis package*. Weierstrass Institute for Applied Analysis and Stochastics, Mohrenstraße 39, 10117 Berlin, Germany.

[13] H. J. Wünsche, U. Bandelow, and H. Wenzel. Calculation of combined lateral and longitudinal spatial hole burning in $\lambda/4$ shifted DFB lasers. *IEEE Journ. of Quant. electron.*, 29(6):1751–1761, 1993.

[14] U. Bandelow, H. Gajewski, and H.-Chr. Kaiser. Modeling combined effects of carrier injection, photon dynamics and heating in Strained Multi-Quantum Well Lasers. to appear in SPIE Proc. of Physics and Simulation of Optoelectronic Devices VIII, 2000.

[15] G. Albinus, H. Gajewski, and R. Hünlich. Thermodynamic design of energy models of semiconductor devices. WIAS Preprint 573, Berlin, 2000.